Electromagnetic response and optical properties of spherical CuSbS2 nanoparticles

PLEASE CITE THE PUBLISHED VERSION

PUBLISHER

IEEE

VERSION

AM (Accepted Manuscript)

PUBLISHER STATEMENT

LICENCE

REPOSITORY RECORD

Electromagnetic Response and Optical Properties of Spherical CuSbS$_2$ Nanoparticles

F. Seyedheydari[1], **K. Conley**[2], **P. Ylä-Oijala**[3], **A. Sihvola**[3], **and T. Ala-Nissila**[1,4]

[1] QTF Center of Excellence, Department of Applied Physics, Aalto University, Finland
[2] Department of Chemistry and Materials Science, Aalto University, Finland
[3] Department of Electronics and Nanoengineering, Aalto University, Finland
[4] Department of Mathematical Sciences, Interdisciplinary Centre for Mathematical Modelling, Loughborough University, United Kingdom

Abstract— We study the electromagnetic response of individual spherical copper antimony disulfide (CuSbS$_2$) nanoparticles and layers embedded with them for solar applications and near-infrared (NIR) sensors using computational methods. We first calculate the single particle scattering and absorption efficiencies using Lorenz-Mie theory. The absorption and the total scattering efficiencies broaden and shift to longer wavelengths with increasing particle radius from 1 to 100 nm. We further investigate the response of multiple nanoparticles embedded in a thin layer at a low volume fraction using a Monte Carlo method. Our results demonstrate that with increasing particle size and scattering NIR transmittance is strongly suppressed and absorption and reflectance enhanced. The high absorption coefficient and solar-compatible band gap of CuSbS$_2$ make it a good candidate for nanocrystalline solar cell and other NIR device applications.

1. INTRODUCTION

Copper antimony disulfide (CuSbS$_2$) is emerging as an alternative solar absorber with earth-abundant constituent elements [1]. Chalcostibite, CuSbS$_2$, is a naturally occurring mineral orthorhombic system with space group *Pnma* [2, 3]. The optical band gap ranges from 1.4 eV to 1.52 eV [4, 5, 6, 7]. For CuSbS$_2$ the fundamental band gaps have been predicted to be indirect in nature; however, the difference between the lowest energy direct and indirect gaps is only of the order of 0.1 eV [8].

In recent years, CuSbS$_2$ thin films deposited by sputtering [9], thermal evaporation [10, 11], or chemical bath deposition [12] have been characterized, but there are only a few studies on the synthesis of CuSbS$_2$ in powder form. In the synthesis of ternary materials, controlling the reaction conditions is essential. Solvothermal, hydrothermal and hot injection methods have already been reported for the formation of CuSbS$_2$ nanocrystals [4, 6, 13, 14, 15]. Most recently, high-quality platelet-like CuSbS$_2$ nanocrystals with a well-defined shape and narrow size distribution were experimentally prepared using an improved hot injection method [7]. This opens up new possibilities to engineer nanoparticle shapes and sizes to best suited for a given application.

In this work, we focus on the fundamental size-dependent optical and NIR properties of CuSbS$_2$ nanoparticles as individual spheres and embedded in a layer at low volume fractions (0.01%). The material properties are described by the complex dielectric function previously calculated using Density Functional Theory (DFT) [16, 17] and Many-Body Perturbation Theory [18].

2. METHODS

Lorenz-Mie scattering of spherical particles: The optical response of a small sphere in an incident electromagnetic field is calculated using Lorenz-Mie theory [19]. In general, the scattered field is a superposition of normal modes, each weighted by the electric, a_n, and magnetic, b_n, Mie coefficients. If the permeability of the particle and the surrounding medium are assumed to be equal, then the electric and magnetic Mie coefficients, a_n and b_n, for a sphere are given by

$$a_n = \frac{\psi_n(x)\psi_n'(m_1 x) - m_1\psi_n'(x)\psi_n(m_1 x)}{\xi_n(x)\psi_n'(m_1 x) - m_1\xi_n'(x)\psi_n(m_1 x)}; \tag{1}$$

$$b_n = \frac{m_1\psi_n(x)\psi_n'(m_1 x) - \psi_n'(x)\psi_n(m_1 x)}{m_1\xi_n(x)\psi_n'(m_1 x) - \xi_n'(x)[\psi_n(m_1 x)}, \tag{2}$$

where the prime indicates differentiation with respect to the argument of the corresponding function. The radial functions $\psi_n(x) = xj_n(x)$, $\xi_n(x) = \psi_n(x) + i\chi_n(x)$ and $\chi_n(x) = -xy_n(x)$ are Riccati-Bessel and Hankel functions where j_n, y_n are the spherical Bessel functions [19]. The size parameter, $x = 2\pi n_m R/\lambda$, R is the radius of sphere, n_m is the refractive index of the surrounding medium, and m_1 is refractive index of the sphere relative to the surrounding medium (n_m). The order of the electric and magnetic modes are represented by n, where dipole corresponds to $n = 1$, quadrupole to $n = 2$, and so on. The total scattering (Q_sca) and absorption (Q_abs) efficiencies [19] can be computed from

$$Q_\mathrm{sca} = \frac{2}{x^2} \sum_{n=1}^{N} (2n+1)(|a_n|^2 + |b_n|^2); \tag{3}$$

$$Q_\mathrm{abs} = \frac{2}{x^2} \sum_{n=1}^{N} (2n+1)[\mathrm{Re}(a_n + b_n) - (|a_n|^2 + |b_n|^2)]. \tag{4}$$

Optical properties of layers containing particles: Monte Carlo simulations provide a method of determining the exact optical properties of thin layers containing large numbers of spheres which is useful for simulating systems with many coupled degrees of freedom. We apply a Monte Carlo method to investigate the optical behavior of the copper antimony disulfide nanoparticles in layers containing spherical particles. The transmittance, reflectance, and absorption of the layer were simulated using a modified Monte Carlo method [20] originally developed by Wang *et al.* [21]. We consider a layer with a thickness $T = 200$ μm embedded with nanoparticles at a volume fraction of $f = 0.01\%$. The particles are embedded in a non-absorbing medium with a refractive index of 1.0 and the layer is surrounded by air. The scattering and absorption coefficients, μ_sca and μ_abs per unit length of the film given by,

$$\mu_\mathrm{sca,abs} = \frac{3}{2} \frac{f \, Q_\mathrm{sca,abs}}{2R}, \tag{5}$$

The ensemble averaged particle asymmetry factor is

$$g = \frac{\sum_i \rho(r_i) \, Q_\mathrm{sca}(r_i) g(r_i)}{\sum_i \rho(r_i) \, Q_\mathrm{sca}(r_i)}, \tag{6}$$

where $\rho(r_i)$ is the particle size distribution, and $Q_\mathrm{sca}(r_i)$ is the scattering efficiency of a particle with radius r_i, and i is the binning index [22]. The effective dielectric permittivity of the layer, ϵ_eff, from Maxwell Garnett Effective Medium Theory is [23],

$$\epsilon_\mathrm{eff} = \epsilon_\mathrm{m} + 3f\epsilon_\mathrm{m} \frac{\epsilon_\mathrm{p} - \epsilon_\mathrm{m}}{\epsilon_\mathrm{p} + 2\epsilon_\mathrm{m} - f(\epsilon_\mathrm{p} - \epsilon_\mathrm{m})}, \tag{7}$$

where ϵ_p and ϵ_m are the dielectric permittivities of the particle and medium components.
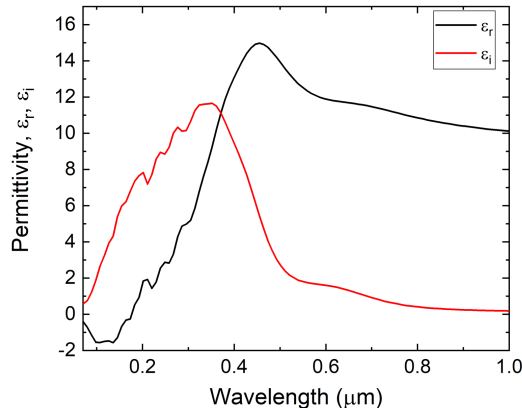

Figure 1: The real and imaginary permittivities of bulk CuSbS$_2$ [16].

The Monte Carlo method used here records the path and termination result of 10^7 photons from an infinitesimally small beam normal to the composite surface. The grid resolution was $dz = 2$ μm and $dr = 1$ μm for the axial and radial directions, respectively.

The real and imaginary components of the permittivity of CuSbS$_2$ used herein were obtained from a previous study using Density Functional Theory [16] and have been averaged over the three orthogonal axes in order to estimate optical properties. Their values are provided in Figure 1.

3. RESULTS AND DISCUSSION

In this section, we discuss results of our calculations from the Lorenz-Mie theory and the Monte Carlo method. The maximum of the absolute value of the dipolar electric and magnetic Mie coefficients modes are in the ultraviolet (UV) to visible regime for particles with a radius less than 100 nm are shown in Figure 2. The electric and magnetic dipole modes broaden and shift to longer wavelength with increasing particle size. The magnitude of the electric modes considerably changes with size. Figure 2 (b) depicts how the magnetic dipole modes redshift when the radius increases but the intensities of these modes for large particles, radii greater than 30 nm here, are more pronounced.
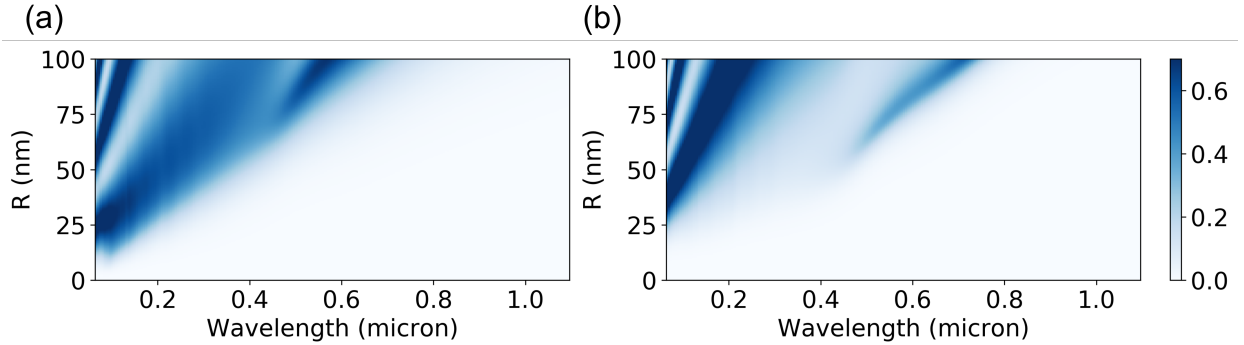

Figure 2: (a) The electric, $|a_1|$, and (b) magnetic, $|b_1|$, dipolar Mie coefficients for CuSbS$_2$ nanoparticles with radius of particles, R, increasing from 1 nm to 100 nm. The refractive index of the surrounding medium is 1.0.

We have explicitly plotted the scattering and absorption efficiencies for a specific radius $R = 100$ nm in Figure 3 (a). We have also plotted the absolute values of first two Mie coefficients, a_1 and b_1, for particle with radius of 100 nm in Figure 3 (a) to investigate the origin of the modes in the scattering efficiency curve. One can clearly see that the peak at the shorter wavelength 0.596 μm in the scattering efficiency is associated with the electric mode and the other one at 0.708 μm with the magnetic mode.

The amplitudes of the scattered electric field corresponding to the maxima of the Mie coefficients are shown in Figure 3. An electric field distribution inside and outside the particle at different wavelengths clearly shows the intensity variation. The high intensity of red color indicates the areas where the magnitude of Q_{sca} is large while the blue color indicates small magnitudes. The electric nearfield in Figure 3 (b) which spatially extends in the inner domain shows that the a_1 mode is characteristic to the dielectric electric dipolar mode [24].
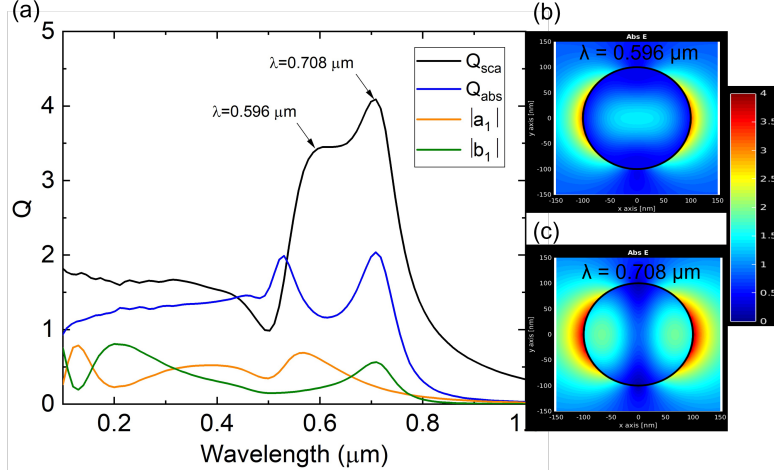
Figure 3: (a) Scattering and absorption efficiencies and Mie coefficients of a sphere of radius 100 nm. Absolute value of the induced electric field at wavelengths 0.596 (b) and 0.708 μm (c).

The absorption, Q_{abs}, and scattering, Q_{sca}, efficiencies of a $CuSbS_2$ particle with radius up to 100 nm in the UV-Visible regime are presented in Figures 4 (a-b), respectively. The intensity of the blue color indicates the magnitude of the efficiencies and the maximum values, corresponding to the electric and magnetic dipolar dielectric resonances, are in dark blue. The dark blue areas of
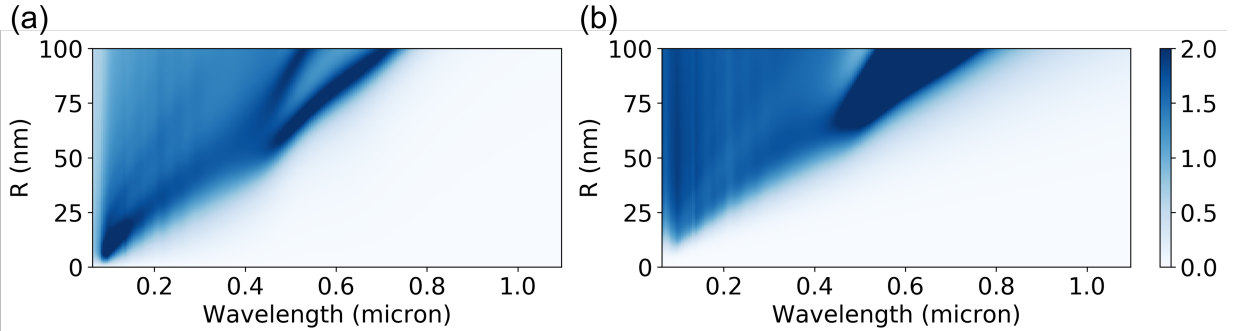

Figure 4: (a) Absorption, Q_{abs}, and (b) scattering, Q_{sca}, efficiencies for $CuSbS_2$ nanoparticles with particle radius up to $R = 100$ nm.

Q_{abs} and Q_{sca} correspond to maxima in the Mie coefficients $|a_1|$ and $|b_1|$ where also the higher order modes are present. As expected from the behavior of the Mie coefficients, Figure 4 (a) indicates that the absorption efficiency maxima broaden and shift to longer wavelengths with increasing particle size. Similarly, the total scattering efficiency broadens and shifts to longer wavelengths with increasing particle size, cf. Figure 4 (b). The modes shift to longer wavelengths because m_1, the relative refractive index of the particle and medium, is larger than one.

Optical properties of compacts embedded with spherical particles: The spectra obtained from Monte Carlo simulations for a 200 μm thick layer embedded with nanoparticles of radii $R = 10, 20, 40, 60, 80,$ and 100 nm at 0.01% volume fraction are shown in Figure 5. When comparing layers having different particle sizes, the data show that there are competing mechanisms between the reflectance and absorption when the transmittance is small. At short wavelengths $\lambda < 0.6$ μm, absorption by the $CuSbS_2$ particles becomes significant enough ($> 90\%$ even at low volume fraction) to be the main transport mechanism. Note that the minimum of absorption is due to the peaks in the reflectance. Regardless of the local variations in the absorption bands in the short-wavelength range, the decrease in the absorption bands occurs at longer wavelengths for a layer containing larger particles.

Increasing the size of the particles embedded in the layers leads to transmittance beginning at longer wavelengths while the intensity of the transmittance decreases in the range considered here $(0.1 - 1.1$ μm$)$. For example for layers containing $R = 10$ nm nanoparticles transmittance begins

at $\lambda = 430$ nm while for $R = 100$ nm this happens beyond 855 nm. The intensity of the reflectance in the layer containing large particles is more pronounced than the intensity in the layer with small ones. In the reflectance curves multiple peaks appear and redshift when the particle size embedded in the layers increases. Subsequently, multiple peaks appear in the absorption curves for layers containing large particles of radii $60 - 100$ nm.
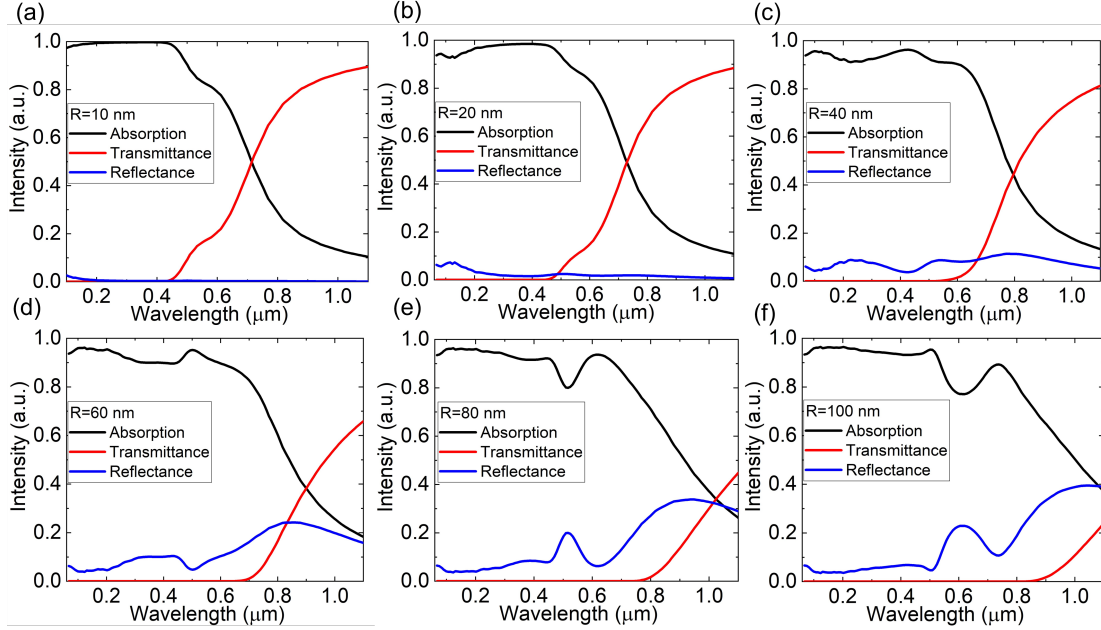

Figure 5: Absorption, transmittance, and reflectance spectra of a 200 μm thick film embedded at 0.01% volume fraction with spherical nanoparticles with $R = 10$ (a), 20 (b), 40 (c), 60 (d), 80 (e), and 100 nm (f).

4. SUMMARY AND CONCLUSIONS

In this work we have studied the scattering and absorption efficiencies of spherical CuSbS$_2$ nanoparticles with radii R up to 100 nm in the NIR regime using Lorenz-Mie theory. The electric and magnetic Mie coefficients of these nanoparticles strongly depend on the particle size. For the large particles the scattering modes redshift and their intensity significantly increases. Furthermore, we have characterized the properties of films of 200 μm in thickness containing spherical particles at a low volume using Monte Carlo methods. The results show how the optical and NIR properties in such layers can be tuned by changing the particle size. For the smallest 10 nm particles the decay of absorption and onset of transmittance rapidly occur around $\lambda = 500$ nm while reflectance remains negligible. With increasing particle size and scattering, transmittance is strongly suppressed and reflectance consequently increases. Such high tunability makes CuSbS$_2$ nanoparticles promising candidates for solar cells and sensors in the NIR regime.

ACKNOWLEDGMENTS

REFERENCES

1. B. Yang, L. Wang, J. Han, Y. Zhou, H. Song, S. Chen, J. Zhong, L. Lv, D. Niu, and J. Tang, "CuSbS$_2$ as a promising earth-abundant photovoltaic absorber material: a combined theoretical and experimental study," *Chem. Mater.*, vol. 26, no. 10, pp. 3135–3143, 2014.

2. E. Peccerillo and K. Durose, "Copper–antimony and copper–bismuth chalcogenides—research opportunities and review for solar photovoltaics," *MRS Energy Sustain.*, vol. 5, pp. 1–59, 2018.

3. K. Takei, T. Maeda, and T. Wada, "Crystallographic and optical properties of CuSbS$_2$ and CuSb(S$_{1-x}$Se$_x$)$_2$ solid solution," *Thin Solid Films*, vol. 582, pp. 263–268, 2015.

4. J. Bincy, G. Silvena G, and R. A. Leo, "Temperature dependent solvothermal synthesis of Cu-Sb-S nanoparticles with tunable structural and optical properties," *Mater. Res. Bull.*, vol. 95, pp. 267–276, 2017.

5. L. Wan, C. Ma, K. Hu, R. Zhou, X. Mao, S. Pan, L. H. Wong, and J. Xu, "Two-stage co-evaporated CuSbS$_2$ thin films for solar cells," *J. Alloys Compd.*, vol. 680, pp. 182–190, 2016.

6. C. Yan, Z. Su, E. Gu, T. Cao, J. Yang, J. Liu, F. Liu, Y. Lai, J. Li, and Y. Liu, "Solution-based synthesis of chalcostibite (CuSbS$_2$) nanobricks for solar energy conversion," *RSC Adv.*, vol. 2, no. 28, pp. 10481–10484, 2012.

7. S. Moosakhani, A. A. S. Alvani, R. Mohammadpour, P.-M. Hannula, Y. Ge, and S.-P. Hannula, "Platelet CuSbS$_2$ particles with a suitable conduction band position for solar cell applications," *Mater. Lett.*, vol. 215, pp. 157–160, 2018.

8. J. T. Dufton, A. Walsh, P. M. Panchmatia, L. M. Peter, D. Colombara, and M. S. Islam, "Structural and electronic properties of CuSbS$_2$ and CuBiS$_2$: potential absorber materials for thin-film solar cells," *Phys. Chem. Chem. Phys.*, vol. 14, no. 20, pp. 7229–7233, 2012.

9. A. W. Welch, P. P. Zawadzki, S. Lany, C. A. Wolden, and A. Zakutayev, "Self-regulated growth and tunable properties of solar absorbers," *Sol. Energy Mater. Sol. Cells*, vol. 132, pp. 499–506, 2015.

10. A. Rabhi, M. Kanzari, and B. Rezig, "Optical and structural properties of CuSbS$_2$ thin films grown by thermal evaporation method," *Thin Solid Films*, vol. 517, no. 7, pp. 2477–2480, 2009.

11. R. Suriakarthick, V. N. Kumar, T. Shyju, and R. Gopalakrishnan, "Effect of substrate temperature on copper antimony sulphide thin films from thermal evaporation," *J. Alloys Compd.*, vol. 651, pp. 423–433, 2015.

12. C. Macías, S. Lugo, Á. Benítez, I. López, B. Kharissov, A. Vázquez, and Y. Peña, "Thin film solar cell based on CuSbS$_2$ absorber prepared by chemical bath deposition (CBD)," *Mater. Res. Bull.*, vol. 87, pp. 161–166, 2017.

13. J. Zhou, G.-Q. Bian, Q.-Y. Zhu, Y. Zhang, C.-Y. Li, and J. Dai, "Solvothermal crystal growth of CuSbQ$_2$(Q= S, Se) and the correlation between macroscopic morphology and microscopic structure," *J. Solid State Chem.*, vol. 182, no. 2, pp. 259–264, 2009.

14. K. Ramasamy, R. K. Gupta, S. Palchoudhury, S. Ivanov, and A. Gupta, "Layer-structured copper antimony chalcogenides (CuSbSe$_x$S$_{2-x}$): Stable electrode materials for supercapacitors," *J. Mater. Chem.*, vol. 27, no. 1, pp. 379–386, 2015.

15. Y. Zou and J. Jiang, "Colloidal synthesis of chalcostibite copper antimony sulfide nanocrystals," *Mater. Lett.*, vol. 123, pp. 66–69, 2014.

16. K. M. Conley, C. Cocchi, and T. Ala-Nissila, "Formation of near-ir excitons in low dimensional CuSbS$_2$," 2021.

17. V. Kumar Gudelli, V. Kanchana, G. Vaitheeswaran, A. Svane, and N. E. Christensen, "Thermoelectric properties of chalcopyrite type CuGaTe$_2$ and chalcostibite CuSbS$_2$," *Int. J. Appl. Phys.*, vol. 114, no. 22, p. 223707, 2013.

18. A. Lawal, L. S. Taura, and M. Madugu, "Quasiparticle effects in bulk and monolayer of CuSbS$_2$ band structure for solar cells and optoelectronic application," *J Sci Educ Technol*, vol. 1, no. 1, pp. 73–79, 2020.

19. C. F. Bohren and D. R. Huffman, *A Potpourri of Particles*, pp. 181–183. Weinheim, Germany: John Wiley & Sons, 1983.

20. J. Tang, V. Thakore, and T. Ala-Nissila, "Plasmonically enhanced reflectance of heat radiation from low-bandgap semiconductor microinclusions," *Sci. Rep.*, vol. 7, p. 5696, 2017.

21. L. Wang, S. L. Jacques, and L. Zheng, "MCML-Monte Carlo modeling of light transport in multi-layered tissues," *Comput. Methods Programs Biomed.*, vol. 47, no. 2, pp. 131–146, 1995.

22. S. Merikallio, *Computer modeling of light scattering by atmospheric dust particles with spheroids and ellipsoids*. PhD thesis, Aalto University, 2016.

23. V. A. Markel, "Introduction to the maxwell garnett approximation: tutorial," *J. Opt. Soc. Am.*, vol. 33, no. 7, pp. 1244–1256, 2016.

24. D. C. Tzarouchis, *Resonant Scattering Particles-Morphological characteristics of plasmonic and dielectric resonances on spherical and polyhedral inclusions*. PhD thesis, Aalto University, 2019.